Nano-Micro Letters

e-ISSN 2150-5551
CN 31-2103/TB

ARTICLE

https://doi.org/10.1007/s40820-025-01982-z

Cite as
Nano-Micro Lett.
(2026) 18:143

Received: 2 July 2025
Accepted: 11 October 2025

TENG-Based Self-Powered Silent Speech Recognition Interface: from Assistive Communication to Immersive AR/VR Interaction

Shuai Lin[1], Yanmin Guo[1], Xiangyao Zeng[1], Xiongtu Zhou[1,2], Yongai Zhang[1,2], Chengda Li[3] ✉, Chaoxing Wu[1,2] ✉

HIGHLIGHTS

- A porous pyramid-structured triboelectric nanogenerator sensor is designed for self-powered silent speech signal acquisition.
- A hybrid neural network that combines convolutional neural network with long short-term memory is proposed to accurately decode silent speech signals.
- Silent speech commands enable real-time, contactless control of smartphones and immersive AR/VR interaction.

ABSTRACT Lip language provides a silent, intuitive, and efficient mode of communication, offering a promising solution for individuals with speech impairments. Its articulation relies on complex movements of the jaw and the muscles surrounding it. However, the accurate and real-time acquisition and decoding of these movements into reliable silent speech signals remains a significant challenge. In this work, we propose a real-time silent speech recognition system, which integrates a triboelectric nanogenerator-based flexible pressure sensor (FPS) with a deep learning framework. The FPS employs a porous pyramid–structured silicone film as the negative triboelectric layer, enabling highly sensitive pressure detection in the low-force regime (1 V N^{-1} for 0–10 N and 4.6 V N^{-1} for 10–24 N). This allows it to precisely capture jaw movements during speech and convert them into electrical signals. To decode the signals, we proposed a convolutional neural network-long short-term memory (CNN–LSTM) hybrid network, combining CNN and LSTM model to extract both local spatial features and temporal dynamics. The model achieved 95.83% classification accuracy in 30 categories of daily words. Furthermore, the decoded silent speech signals can be directly translated into executable commands for contactless and precise control of the smartphone. The system can also be connected to AR glasses, offering a novel human–machine interaction approach with promising potential in AR/VR applications.

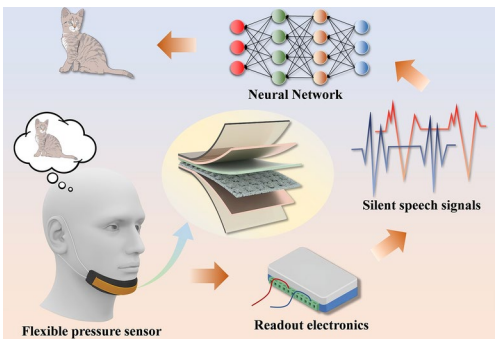

KEYWORDS Flexible pressure sensor; Silent speech recognition; Triboelectric nanogenerator; Deep learning; AR/VR interaction

Shuai Lin and Yanmin Guo have contributed equally to this work.
✉ Chengda Li, lichengda@xmcu.edu.cn; Chaoxing Wu, chaoxing_wu@fzu.edu.cn
[1] School of Physics and Information Engineering, Fuzhou University, Fuzhou 350108, People's Republic of China
[2] Fujian Science & Technology Innovation Laboratory for Optoelectronic Information of China, Fuzhou 350116, People's Republic of China
[3] School of Artificial Intelligence, Xiamen City University, Xiamen 361008, People's Republic of China

Published online: 12 January 2026

Shanghai Jiao Tong University Press

Springer

1 Introduction

Language, the cornerstone of human connection, is essential for expressing thoughts and building social bonds [1–3]. Yet, for millions with speech impairments due to neurological disorders, brain injuries, or congenital conditions [4–14], the inability to vocalize severely limits social participation and access to services [15]. Silent speech technologies, particularly lip-based communication, offer a critical alternative for these individuals to reclaim their voice.

Lip language provides a natural, intuitive, and hands-free means of silent speech communication [16–19]. Importantly, its articulation involves not only the lips but also the jaw and the muscles surrounding it, whose kinematic patterns carry essential information for recognizing silent speech. Despite its potential, accurately capturing and decoding these subtle articulatory movements remains a significant technical challenge, especially in real-world conditions.

Currently, silent speech recognition (SSR) methods mainly include vision-based, electromyography (EMG)-based, and radar-based techniques, which have achieved significant breakthroughs in recent years. Vision-based methods have leveraged multimodal fusion and deep learning, such as Yu et al.'s cascade fusion algorithm with pre-trained Visual-HuBERT for integrating tongue and lip features [20], and Wang et al.'s PointVSR model using depth-sensed point cloud data from multiple sensor positions [21]. EMG-based methods have explored novel combinations of time–frequency features, deep learning architectures, and signal-to-image transformations, including Huang et al.'s GRU-based modeling on a Chinese word corpus [22] and Li et al.'s SVIT-SSR framework employing Vision Transformers [23]. Radar-based methods have demonstrated the potential of non-contact recognition. Menezes et al. explored continuous phoneme recognition with radar signals using feature combinations and CNN-MLP models [24], and further investigated on-body antenna configurations to optimize multi-speaker recognition [25]. These studies collectively highlight recent innovations in multimodal fusion, model design, and non-contact recognition, providing a foundation for advancing SSR technologies.

However, each method has its own application scenarios and challenges. Vision-based method provides rich articulatory information in well-lit, unobstructed environments, achieving high accuracy, but is susceptible to lighting variations and occlusion. EMG-based method achieves high sensitivity by detecting muscle activity directly, yet requires skin-attached electrodes and external power. Radar-based method enables non-contact detection and can operate under low-light or occluded conditions, although its spatial resolution is moderate and it is sensitive to electromagnetic interference (Table S1).

Since it was first proposed in 2012 [26, 27], the triboelectric nanogenerator (TENG) has rapidly become a technology of great interest due to its unique self-powered characteristics, low cost, and easy fabrication [28–31]. TENG converts mechanical energy into electrical energy through the principle of the triboelectric effect and electrostatic induction, showing potential application in human–machine interaction [32–36]. For example, by using this technology, accurate recognition of large-range joint motions can be achieved, enabling self-powered control of robotic devices through neck gestures [37]. Due to its high sensitivity, self-powered operation, and wearable compatibility, TENG shows strong potential for applications in real-time silent speech recognition.

Here, we report a real-time silent speech recognition system (RT-SSRS) that integrates a self-powered flexible pressure sensor (FPS) based on TENG with a deep learning framework. The FPS employs a porous pyramid-structured silicone (PPS) film as the negative triboelectric layer, designed to precisely capture jaw movements during speech. To decode these complex spatiotemporal signals, we proposed a hybrid neural network that combines convolutional neural network (CNN) for spatial feature extraction with long short-term memory (LSTM) for capturing temporal dynamics. This model achieves a classification accuracy of 95.83% across 30 daily words. Furthermore, we demonstrate the practical utility of RT-SSRS in real-world human–machine interaction scenarios, translating silent speech commands into contactless smartphone control actions. The system can also be connected to AR glasses, demonstrating a potential prototype for future human–machine interaction in AR/VR applications. Compared to other methods, our TENG-based approach demonstrates high sensitivity to subtle pressure variations, lightweight and comfortable wearable design, self-powered operation, and excellent environmental robustness (Table S1). Moreover, all components of our sensor are made from common, low-cost materials, providing biocompatibility, mechanical flexibility, and scalability. These characteristics make it highly suitable for integration into

https://doi.org/10.1007/s40820-025-01982-z

AR/VR interaction systems. With further optimization in the future, we believe there will be further breakthroughs in accuracy and other aspects. Overall, the RT-SSRS ensures reliable silent speech recognition for speech-impaired users, reduces communication burden, and offers a novel human–machine interaction approach with broad application prospects and significant societal value.

2 Experimental Section

2.1 Fabrication of the PPS Film

The PPS film was prepared using a simple and efficient sacrificial NaCl template method. First, component A and component B of Ecoflex 00–30 were mixed in a 1:1 weight ratio. Subsequently, NaCl particles were added to the prepared Ecoflex mixture in a 1:1 weight ratio with continuous stirring for 20 min to allow for thorough mixing. Next, the stirred Ecoflex-NaCl mixture was poured into a mold with a pyramidal structure and vacuumed to completely remove air bubbles. The mixture was then cured on a heating table at 60 °C for 1 h to ensure that the mixture was fully cured and a stable pyramid structure was formed. Once curing was complete, the Ecoflex-NaCl mixture was carefully peeled from the mold using tweezers and immersed in deionized water for 12 h, during which time the water was changed periodically to accelerate the dissolution of the NaCl particles, resulting in the formation of a porous structure. Finally, the soaked samples were thoroughly rinsed with deionized water to remove residual salts and other impurities. After cleaning, the samples were dried in an oven at 100 °C for 12 h to ensure that their internal water was completely evaporated, and finally PPS film were obtained.

2.2 Fabrication of the FPS

The PPS film and nylon were used as the negative and positive triboelectric layers, respectively, and were cut into rectangular pieces with dimensions of 2 cm × 8 cm. Then, copper foils of the same size were pasted as electrodes, and a conductive copper wire was led out from each of them to facilitate the connection with external circuits. Next, the PPS film was placed opposite to the nylon, and the entire sensor was encapsulated with a polyimide (PI) film to mitigate the effects of the external environment during use while maintaining its flexibility and durability. Finally, a 3 cm × 16 cm piece of fabric was cut, rubber bands were tied at both ends, and the FPS was fixed to the fabric.

2.3 Characterization and Measurements

A linear motor (LinMot B 01–37 × 166/260) was used to generate periodic reciprocating motion for applying pressure. The pressure magnitude was adjusted by varying the movement distance and measured using a force gauge (ZNLBM-IIX-20 KG). A programmable electrometer (Keithley 6514) was employed to measure output voltage. Silent speech signals were acquired using an NI 1252A readout electronic on the PyCharm platform. The CNN-LSTM model was developed based on the PyTorch framework and trained on a GeForce RTX 4070 GPU. The UI interface is designed based on PyQt, and the mobile application is developed using App Inventor.

3 Results and Discussion

3.1 Design of the RT-SSRS and the FPS

The architecture of RT-SSRS is shown in Fig. 1a. The RT-SSRS consists of a FPS, a readout electronic, and a neural network. The FPS is worn on the chin and is capable of converting pressure variations caused by muscle movements into electrical signals. The readout electronic module is responsible for transmitting the signals. Finally, the signals are input into a trained neural network model, enabling precise and real-time decoding of silent speech signals.

Recent research advancements have highlighted the critical importance of microstructural engineering in enhancing the performance of flexible electronic devices. As systematically reviewed by Huang et al., the importance of microstructural engineering in flexible metamaterial electronics provides key design guidelines for achieving high-performance sensing [38]. Here, we fabricated FPS by combining PPS film with copper foil, nylon and polyimide (PI) in the structure shown in Fig. 1b. PPS film is used as the negative triboelectric layer, which has excellent triboelectric electrical properties, elasticity, durability and biocompatibility, and can be customized with different

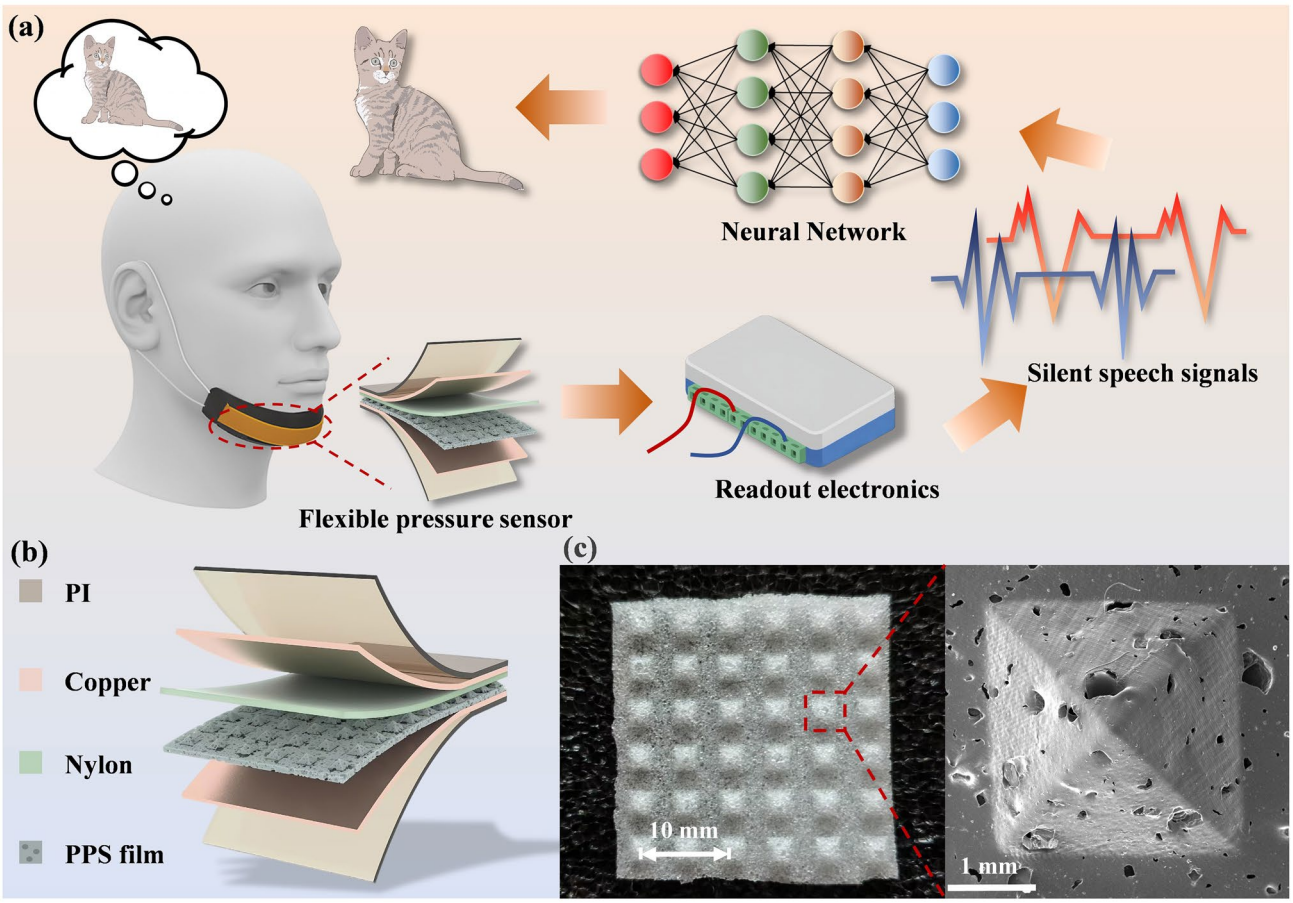

Fig. 1 Design of the RT-SSRS and the FPS. **a** Overall architecture of the RT-SSRS. **b** Schematic representation of the structure of the FPS. **c** Top view and SEM image of the PPS film

surface morphologies. Nylon is used as a positive triboelectric layer because it shows the highest output voltage in triboelectric electrical performance test. Copper foil is used as an electrode, and PI is used to encapsulate the entire sensor to reduce interference from sweat and human body potential. The materials used are low-cost and easy to process for mass production, and the sensor is lightweight and comfortable to wear with little extra burden.

This study employs a simple and efficient sacrificial NaCl templating method for the preparation of PPS film (Fig. S1). First, NaCl was thoroughly mixed with Ecoflex 00–30 material and poured into a pyramid-structured mold for curing. The PPS film is subsequently obtained by dissolving the NaCl particles and drying the material. The detailed steps of this preparation process are described in the experimental section. The PPS film can be stretched and twisted (Fig. S2), indicating its good mechanical properties. The PPS film is illustrated in Fig. 1c, which includes a top-view image showing a uniformly distributed pyramid structure that deforms under external forces, and an SEM image revealing a porous microstructure that helps reduce its elastic resistance. The film exhibits excellent mechanical and triboelectric properties, enabling it to detect subtle pressure variations.

The working principle of FPS adopts the contact separation mode (Fig. S3). The whole cycle is divided into four stages: first, when the muscle squeezes the FPS, the PPS film comes into contact with the nylon. Owing to the different electronegativity of the two triboelectric layers, negative triboelectric charges are generated on the PPS film side, while positive triboelectric charges are generated on the nylon side (Stage 1). When the muscle contracts, the two triboelectric layers

 https://doi.org/10.1007/s40820-025-01982-z

begin to separate, and due to the potential difference generated by electrostatic induction, which drives electrons to flow in the external circuit from the PPS film electrode to the nylon electrode (stage 2). Until the muscle completely contracts, the external force disappears, and the two triboelectric layers reach the maximum separation distance (stage 3). When the muscle starts to squeeze the FPS again, the two triboelectric layers come close to each other, driving the flow of electrons from the nylon side to the PPS film side, generating a reverse current (stage 4). Once the muscle completely squeezes the FPS, this cycle returns to stage 1, completing one cycle. It can be seen that the FPS is self-powered and does not require an external power source to generate a voltage output, which is one of its main advantages over other sensors.

3.2 Electrical Characteristics of the FPS

The surface structure of FPS has a significant impact on its pressure response characteristics. We fabricated silicone films as the negative triboelectric layer with different surface structures using various molds, with nylon as the positive triboelectric layer. First, we compared the open-circuit voltage of FPS with flat and pyramid structures under the same pressure (29 N). As shown in Fig. 2a, the output voltage of pyramid structure (31 V) is about four times that of the flat structure (8 V). This result can be attributed to the following factors: (1) This is because the capacitance change in the deformation process is significantly improved due to the presence of the air voids and the increase in effective dielectric constant [39]. (2) In the structured films, the triboelectric charges are more easily separated and thus a larger dipole moment will form between the electrodes [40].

Figure 2b shows the pressure response curves of FPSs with different surface structures (pyramid and hemisphere). The output voltage increases with pressure, as higher pressure deforms the surface, enlarging the contact area between triboelectric layers and generating more charges. The curves exhibit several nearly linear intervals. In the 0–10 N range, the pyramid structure shows higher sensitivity (0.58 V N^{-1}) than the hemisphere structure (0.33 V N^{-1}). In the 10–35 N range, both sensitivities increase, with the pyramid structure (2.8 V N^{-1}) remaining superior to the hemisphere structure (1.67 V N^{-1}). Beyond 35 N, the pyramid structure saturates due to full deformation, while the hemisphere structure continues to rise steadily owing to its higher elastic resistance.

To further investigate the effect of surface geometry, three pyramid-structured FPSs with different sizes and densities were fabricated: (1) small-size, low-density (1.5 mm height, 3 mm width, 3 × 3 array), (2) large-size, low-density (2 mm height, 4 mm width, 3 × 3 array), and (3) small-size, high-density (1.5 mm height, 3 mm width, 4 × 4 array). The small-size, low-density structure corresponds to that in Fig. 2b. As shown in Fig. 2c, the size and density of the FPS affect both its sensitivity and pressure range. A trade-off must be considered for practical applications. For silent speech recognition, we selected the small-size, low-density structure, as it offers the highest sensitivity while maintaining a suitable pressure range for this scenario.

As can be seen, adjusting the shape, size, and density of surface structures can reduce elastic resistance and increase voltage output under the same pressure. However, the accompanying reduction in overall surface area limits the growth of effective contact area, resulting in only modest improvements in pressure sensitivity. To overcome this limitation, we fabricated a porous structure based on the small-size, low-density pyramid design. This approach not only lowers elastic resistance but also increases the specific surface area [41], significantly enhancing pressure sensitivity. As shown in Fig. 2d, the porous pyramid exhibits markedly higher sensitivity than the non-porous counterpart (1 V N^{-1} for 0–10 N and 4.6 V N^{-1} for 10–24 N), with an overall response range of 0–24 N, making it suitable for silent speech signal acquisition.

The triboelectric properties of the positive layer directly influence the efficiency of charge generation. Figure 2e compares the output voltage of FPSs using different materials as the positive triboelectric layer. Nylon exhibits a significantly higher output voltage than other materials, due to its stronger tendency to lose electrons in the triboelectric series, generating more charges during contact–separation. Therefore, nylon was chosen as the positive triboelectric material.

In practical applications, sweat on the skin surface may affect the triboelectric properties of the FPS. Figure 2f shows the output voltage of the FPS as the amount of artificial sweat increases. The FPS exhibited a slight voltage drop, verifying its suitability for use in high-humidity environments. In addition, temperature-dependent tests (Fig. S4) reveal that the output voltage slightly increases with rising temperature but remains overall stable. Since the FPS is worn in close

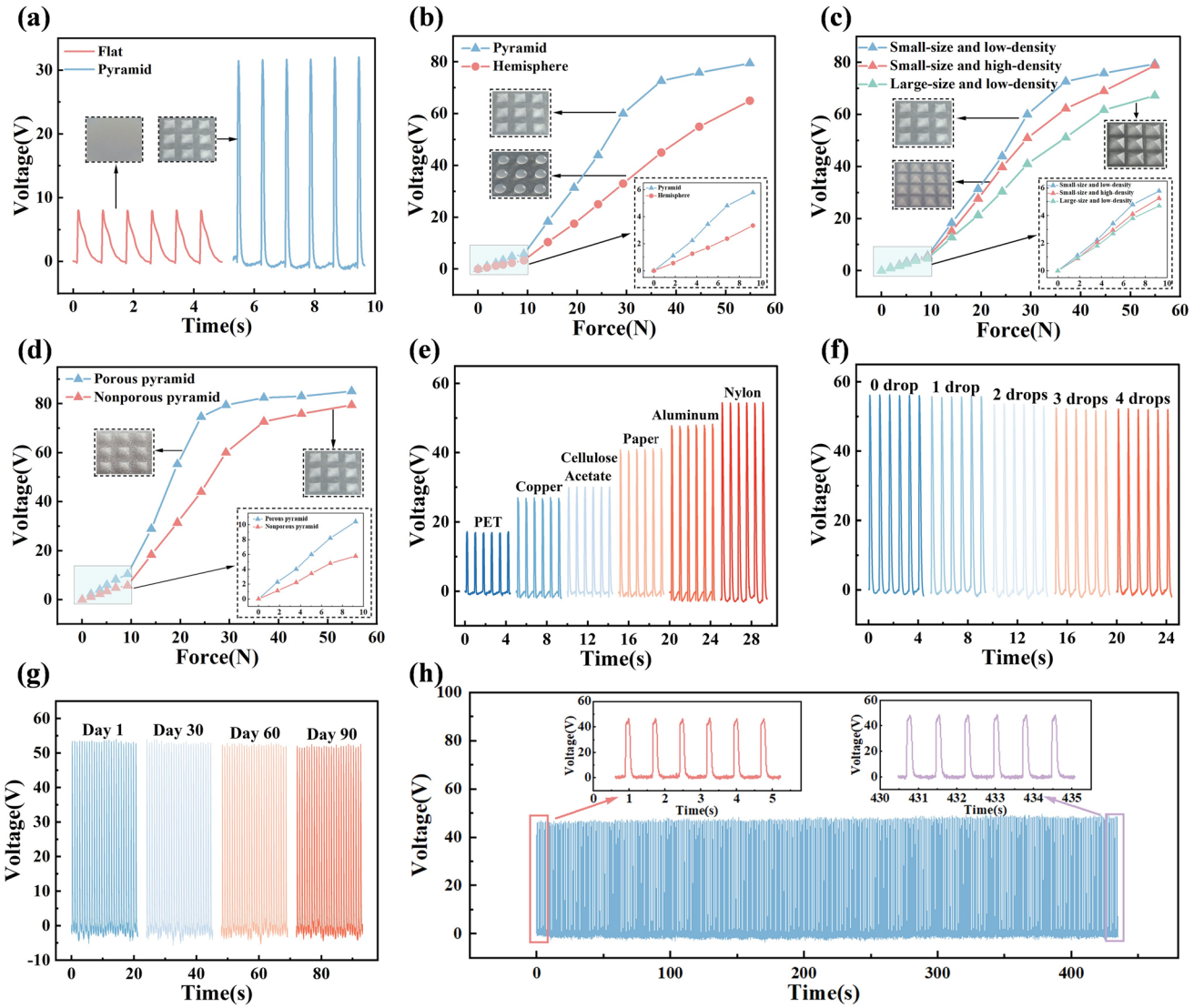

Fig. 2 Electrical characteristics of FPS. **a** Comparison of open-circuit voltage between pyramid and flat structures under the same pressure. **b** Pressure response of pyramid and hemisphere structures. **c** Pressure response of pyramid structures with different sizes and densities. **d** Pressure response of porous pyramid structure and non-porous pyramid structure. **e** Output voltage of FPS using different positive triboelectric materials. **f** Output voltage of FPS under different amounts of artificial sweat. **g** 90 days durability test. **h** 580 cycles stability test

contact with the human body, the temperature variations are limited; within the physiological range of 23.6–42.3 °C, the output voltage remains stable, further demonstrating reliable performance under practical thermal conditions.

To further assess the long-term reliability of the FPS, a 90-day endurance test was conducted, with output voltage measured at 1, 30, 60, and 90 days. The voltage remained stable (Fig. 2g), and after 580 contact–separation cycles, the output was well maintained (Fig. 2h). SEM images of the pyramid structures after cycling (Fig. S5) show that the morphology remains intact without noticeable deformation. Considering that the FPS is mainly used to detect jaw and surrounding muscle movements in silent speech recognition, which involve relatively low and intermittent pressures, the pyramid structures are unlikely to experience significant stress, further ensuring long-term stability.

3.3 Acquisition and Analysis of Silent Speech Signals

During actual speech, jaw movements and local muscular activities exert pressures on the FPS surface, driving the

https://doi.org/10.1007/s40820-025-01982-z

contact–separation process of the triboelectric layers and thereby inducing dynamic charge transfer. Specifically, jaw closing or local muscle contraction, corresponding to the separation process (Stages II–IV in Fig. S3), drive electrons from the PPS film electrode to the nylon electrode. If the PPS film electrode is defined as the positive terminal, this results in a negative voltage spike. In contrast, jaw opening or muscle relaxation, corresponding to the contact process (Stages IV–II in Fig. S3), induce electron transfer in the opposite direction, and generate a positive spike. Consequently, the sequence of jaw motions is directly converted into a characteristic voltage waveform. The resulting voltage waveform accurately reflects the temporal characteristics of muscle movements during speech, providing a reliable electrical signal foundation for subsequent speech pattern recognition and classification.

In order to investigate the characteristics of the silent speech signals captured by FPS, we analyzed 30 categories of daily words as representative samples for analysis. To ensure the validity and accuracy of the subsequent analysis, the silent speech signals were preprocessed to preserve the original signal characteristics and reduce the interference from external factors. First, the raw signals were passed through a low-pass filter with a cutoff frequency of 20 Hz to filter out work-frequency interference and other high-frequency noise. Next, the baseline was removed to eliminate slow drift due to environmental changes or physiological factors to ensure signal stability. Figure 3a–f shows the preprocessed silent speech signals for six selected categories, while signals for all 30 categories are shown in Fig. S6.

It is worth noting that to achieve real-time performance and portability, we employed a data acquisition (DAQ) card to replace electrometers for signal acquisition, which resulted in a reduction in signal amplitude (Note S1 and Fig. S7). Furthermore, the output voltage waveforms acquired initially and after 10 h of wear exhibit high consistency without noticeable deformation (Fig. S8). This demonstrates that the FPS can ensure stable signal acquisition and reliable performance during extended use.

As shown in Fig. 3g, the word “Koala” can be divided into multiple stages, with jaw contractions, openings, and closures producing characteristic positive and negative spikes. During Stage 1, the subject prepares to pronounce the syllable, and the signal remains at baseline. Stage 2, preparing /kəʊ/, shows a significant negative spike due to initial muscle contraction. Stage 3, during /kəʊ/ emission, produces prominent positive spikes from mouth opening and associated muscle activity. Stage 4, immediately after /ɑː/, exhibits a second positive spike before returning toward baseline. Stage 5, during the transition to /lə/, shows a negative spike from oral cavity closure. Stage 6, pronouncing /lə/, generates small positive spikes. Stage 7, at the end of articulation, produces small negative spikes as the mouth closes. Stage 8, after pronunciation completion, sees muscle activity cease and the signal return to baseline. This confirms that the FPS is capable of reliable mapping between articulation dynamics and electrical signals.

In order to further understand the silent speech signals, we constructed a database containing 120 samples for each class. We chose three shallow features, duration, spectral centroid and peak-to-peak value, for statistical analysis of the samples in the database. Figure 3h shows the ridge plot of the peak-to-peak value feature. It can be seen that the distribution differences between some categories are significant. For example, “Banana” is predominantly distributed around 0.26 V, while “Grab” is concentrated around 0.14 V. However, there is significant overlap in the distribution of other categories such as “Toilet” and “Zero”, which are predominantly distributed around 0.075 V. The same is true for duration and spectral centroid (Fig. S9), where the distributions of certain categories show some differentiation, but there are also many categories with varying degrees of overlap between them. Therefore, classification of silent speech signals cannot be effectively performed by simply setting thresholds for these surface features.

To further investigate the similarity of silent speech signals in the database, we employed Dynamic Time Warping (DTW) distance as a metric. DTW effectively handles nonlinear distortions and differences in sequence length, making it suitable for evaluating silent speech signal similarity. Taking "Apartment" and "Umbrella" as examples. As shown in Fig. 3i, the DTW distance between the "Apartment" samples (1.47) is smaller than that between "Apartment" and "Umbrella" samples (2.68), indicating higher similarity within the same category. We then computed average DTW distances across all categories (Fig. S10). The diagonal elements are the smallest in their respective rows and columns, confirming that intra-class similarity is higher than inter-class similarity. This demonstrates the stability of the FPS and its effectiveness in capturing distinctive silent speech features. However, some category pairs exhibit relatively low average DTW distances, with the minimum reaching 1.1, suggesting high similarity that could lead to

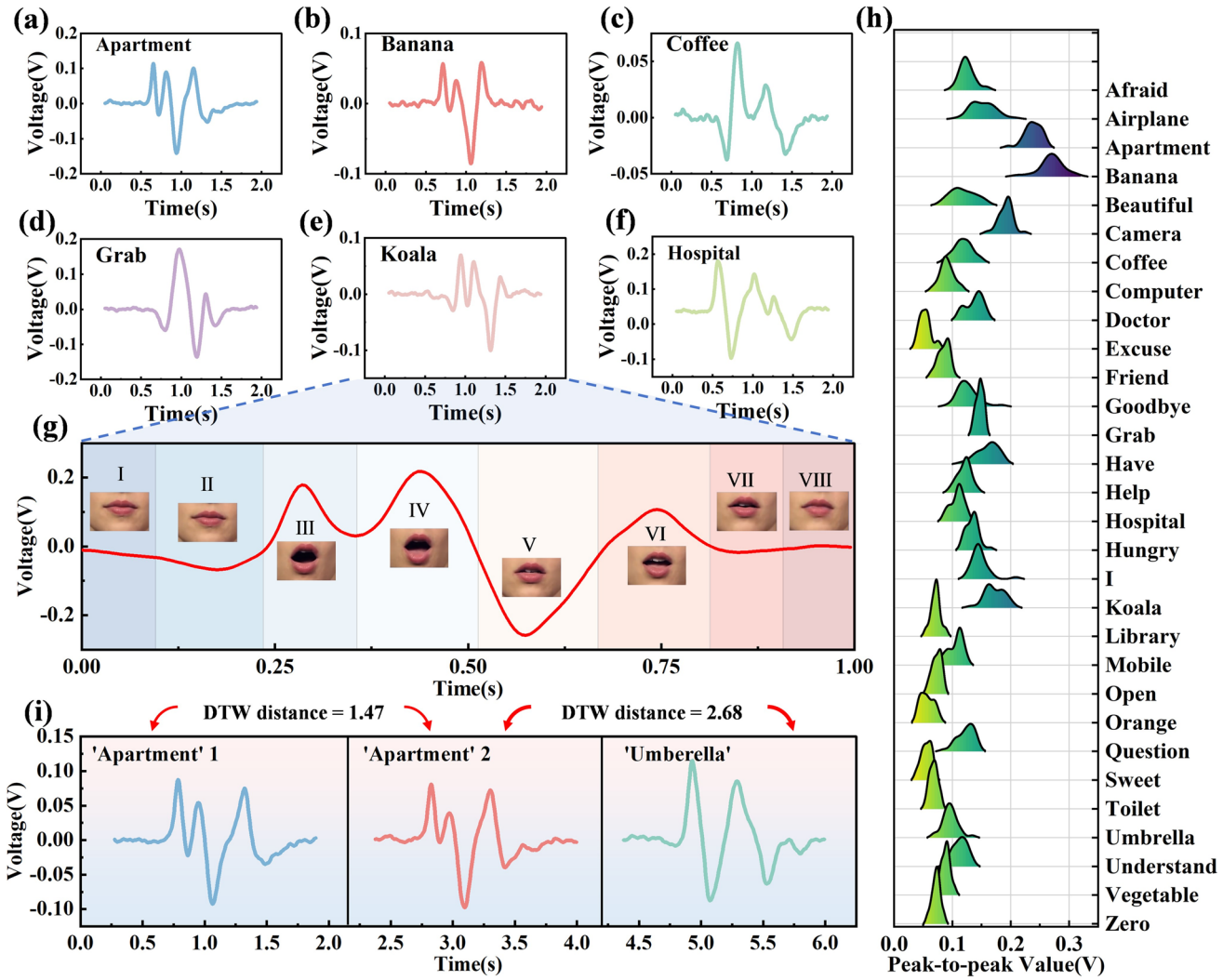

Fig. 3 Acquisition and analysis of silent speech signals. **a-f** Preprocessed waveforms of six selected silent speech signals. **g** Correspondence between silent speech signal and mouth movements, divided into eight phases for "Koala" as an example. **h** Ridge plot of peak-to-peak feature of silent speech signals. **i** Comparison of DTW distances between intra-class ("Apartment" and "Apartment") and inter-class ("Apartment" and "Umbrella")

classification errors. These findings highlight the need for more advanced classification methods to further improve silent speech recognition performance.

3.4 Design and Performance of the Neural Network

As analyzed above, some classes of voltage signals exhibit high similarity. Therefore, ensuring clear and accurate classification of different words has been one of our primary challenges, which is why we introduce the neural network. To further improve recognition performance, we developed a hybrid neural network combining convolutional neural network (CNN) and long short-term memory (LSTM), which enables extraction of both local spatial features and temporal dynamic patterns of the signals. Instead of simply comparing waveform similarity, the model takes into account statistical indicators such as mean, variance, and power spectral density, thereby capturing deeper mappings between different wave forms and their corresponding vocabularies. Because of this approach, even if two wave forms present similar signal patterns, the statistical differences allow us to accurately determine their respective words. For more complex and highly similar vocabularies, future work may require

 https://doi.org/10.1007/s40820-025-01982-z

leveraging contextual information together with large language models to address the issue.

The structure of the CNN-LSTM is shown in Fig. 4a. It mainly consists of three modules: the CNN block, the LSTM block, and the classification block. The CNN block serves as the front end, capturing local features within a short time window, such as waveform peaks, valleys, and slopes. The LSTM block, whose unit structure is shown in Fig. 4b, receives the extracted features from the CNN block and performs dynamic temporal modeling. Finally, the processed features are passed to the classification block, where a fully connected layer maps them to the output space, and a softmax activation converts the results into a probability distribution.

The dataset is crucial to the performance of the neural network, and the process of creating the dataset is as follows: Take "Koala" for example, participants were asked to say "Koala" once every 2 s, 30 times for each group, 10 groups in total. Then, the data were preprocessed (filtered and de-baselined). Finally, the overlapping sliding window is applied to segment the data.

To evaluate the effectiveness of the overlapping sliding window, we applied different step sizes to the training set and tested the resulting CNN–LSTM performance (Fig. 4c). As the overlap ratio increased, test accuracy gradually improved, peaking at 95.83% with a 75% overlap. However, further increasing the overlap to 87.5% reduced accuracy to 94.44%. This demonstrates that overlapping windows effectively increase the number of training samples and improve the robustness of the model. Nevertheless, overly small step sizes introduce redundant samples, leading to overfitting and higher computational costs. Based on this trade-off, we selected a 100-step window (75% overlap), which balances data augmentation and sample diversity while avoiding redundancy.

To validate the contribution of the LSTM module, we compared CNN and CNN-LSTM in classifying 30 daily words. As shown in Fig. 4d, both models' validation accuracy curves converge rapidly, but CNN-LSTM achieves a higher final accuracy of 94.17% compared to 88.33% for CNN, demonstrating its superior performance. To further evaluate the models' dependence on training set size, we gradually reduced the training samples to 100%, 80%, 60%, 40%, and 20%. While accuracy declines for both models with fewer samples, CNN-LSTM remains more stable, maintaining 83.06% accuracy at 20% of the training data, whereas CNN drops to 60.00% (Fig. 4e). The t-distributed Stochastic Neighbor Embedding (t-SNE) visualization of the high-dimensional feature space shows that CNN-LSTM achieves better intra-class compactness and inter-class separability than CNN (Figs. 4f and S11a). Finally, the confusion matrix of CNN-LSTM indicates an average accuracy of 95.83%, with 17 categories reaching 100% and 11 categories above 91.7%, whereas CNN achieves only 90.28% on average with a minimum accuracy of 66.7% (Figs. 4g and S11b). These results consistently demonstrate that incorporating LSTM substantially enhances classification of silent speech signals acquired by the FPS.

To further evaluate the generalization capability of the proposed RT-SSRS, we conducted cross-individual experiments. A supplementary dataset comprising 10 daily phrases (e.g., "nice to meet you," "thank you," "see you later") was acquired from three participants. Representative signals are provided (Fig. S12). And the recognition results reveal that the system achieved an average cross-individual accuracy of 91.13% across all phrase categories, with distinct clustering of signals corresponding to different phrases (Fig. S13). These results underscore the potential of the proposed approach for deployment in real-world multi-user scenarios.

Although the RT-SSRS demonstrates strong performance in individual scenarios, its cross-individual accuracy (91.13% for 10 daily phrases across three individuals) reveals the challenge of generalization. However, this result also demonstrates its potential for multi-user applications. Future work will focus on further improving the generalization and robustness of the proposed system. On the hardware side, developing higher-sensitivity sensors will facilitate the capture of subtle biomechanical variations across different users. On the algorithmic side, advanced strategies such as transfer learning, speaker adaptive modeling, and domain generalization are expected to enhance cross-individual performance.

3.5 Application of the RT-SSRS

To demonstrate the practical application of the RT-SSRS in human–machine interaction, we implemented a prototype system as shown in Fig. 5a. When the user utters a command, RT-SSRS recognizes and decodes the signal in real time, displays the result on the interface, and transmits the

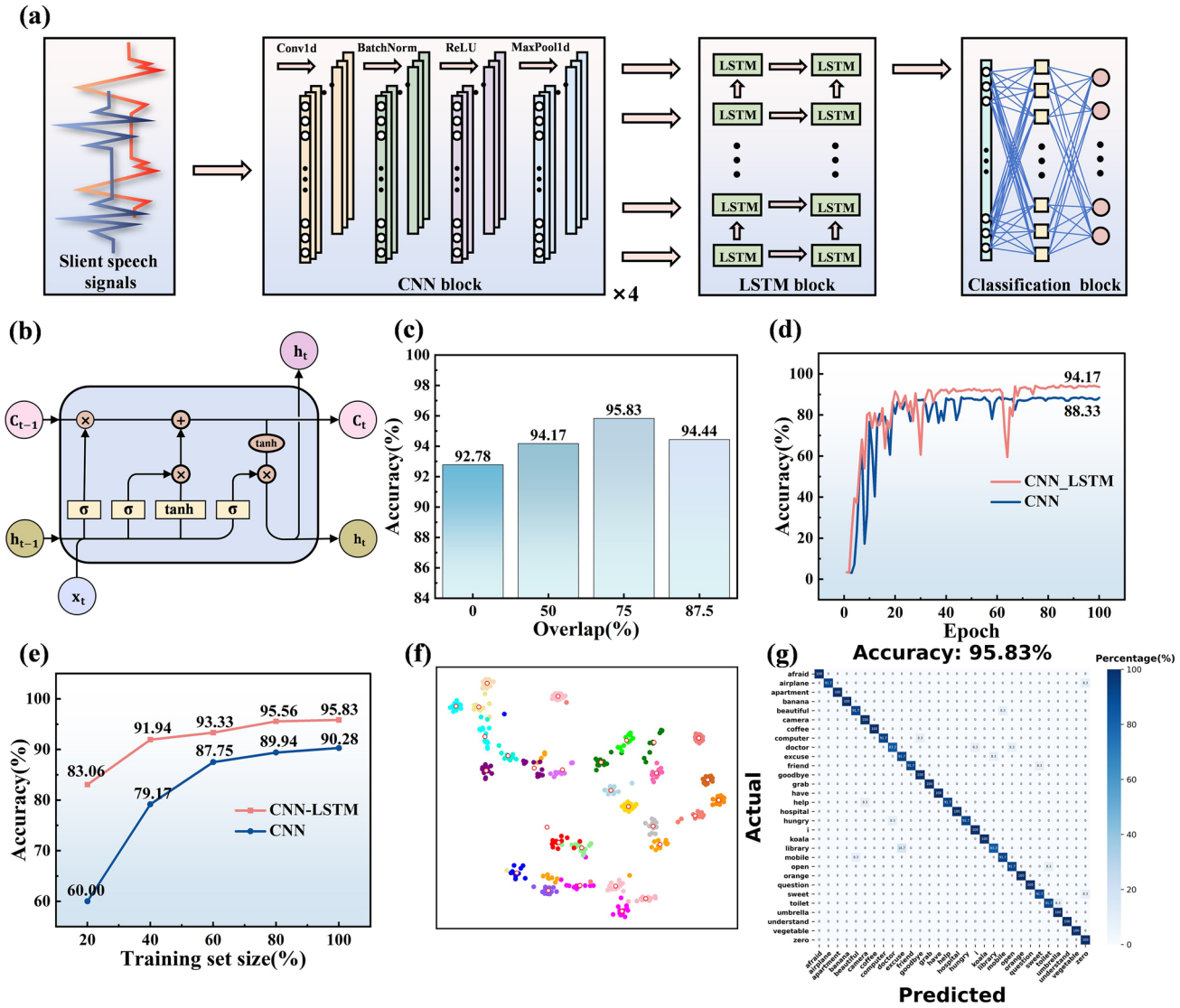

Fig. 4 Design and performance of the CNN-LSTM neural network. **a** Schematic diagram of the structure of the CNN-LSTM. **b** The internal structure of the LSTM unit. **c** Accuracy under different sliding window step sizes. **d** Validation accuracy curves of CNN and CNN-LSTM during training. **e** Accuracy of the CNN-LTM under different training set sizes. **f** t-SNE visualization of feature embeddings from the CNN-LSTM. **g** Confusion matrix of the CNN-LSTM for 30 categories of daily words

command to the smartphone via Bluetooth for execution, thereby enabling precise and contactless control. As shown in Fig. 5b, the computer interface displays both the real-time raw signals and the processed waveforms, along with the recognized command output. Figure 5c shows the mobile application interface, which performs the corresponding operation based on the received command. We implemented three representative functions: "Open camera," "Make a call," and "Open FZU." The CNN-LSTM model achieved a classification accuracy of 97.22% for these commands on the test set, as illustrated by the confusion matrix in Fig. 5d. The waveform analysis in Fig. 5e demonstrates high intra-class consistency and clear inter-class distinction, confirming the system's reliability.

A demonstration video is provided in Movie S1. As noted in Sect. 3.3, the use of a portable DAQ card resulted in a reduction of signal amplitude. Therefore, to ensure robust signal acquisition for demonstration and to better illustrate

https://doi.org/10.1007/s40820-025-01982-z

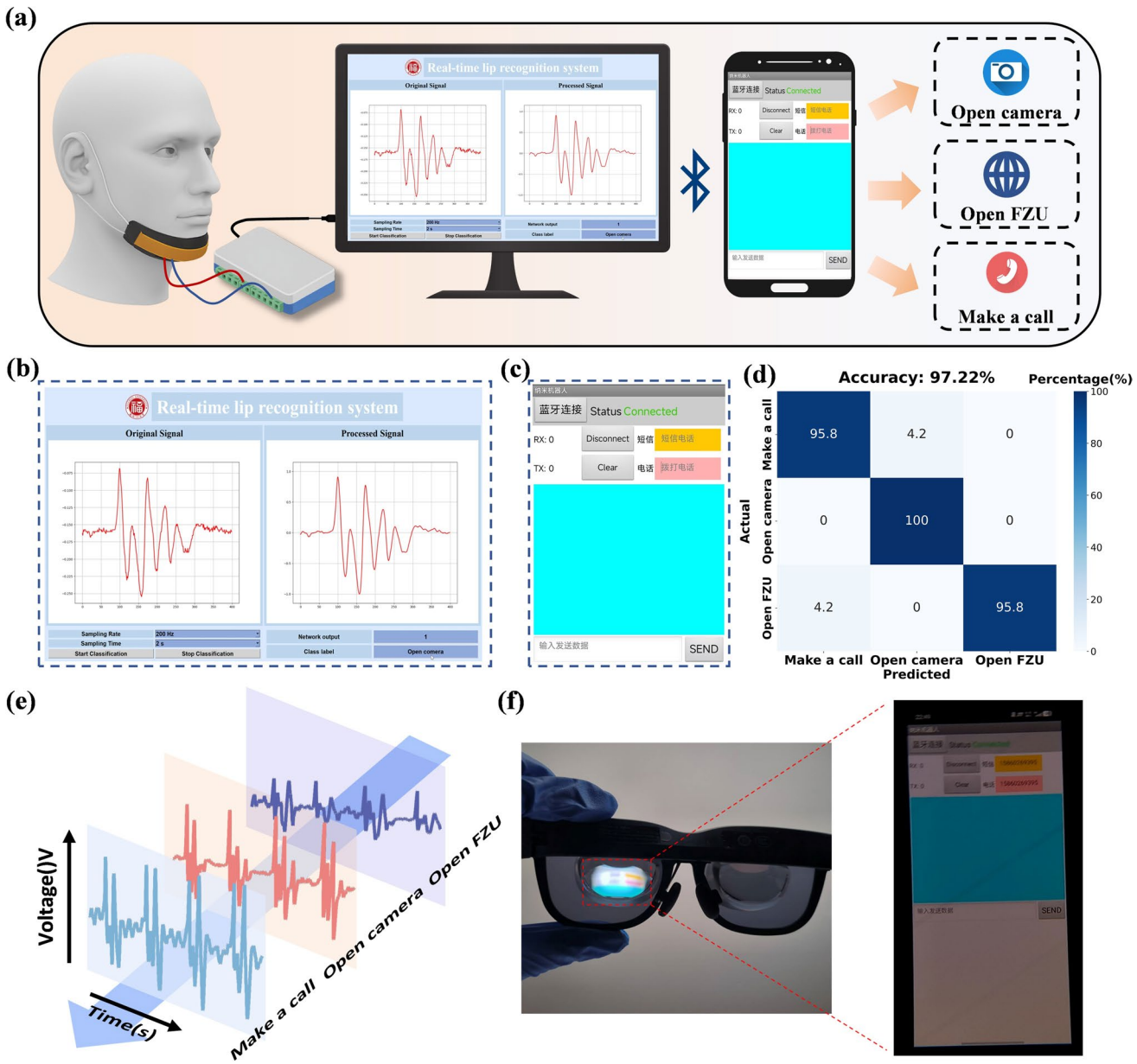

Fig. 5 Application of the RT-SSRS. **a** Schematic illustration of RT-SSRS in a human–machine interaction scenario. **b** Computer interface displaying raw and processed signals along with recognition results. **c** Mobile application interface executing commands such as "Open camera," "Make a call," and "Open FZU." **d** Confusion matrix for the three command words. **e** Waveforms of the three commands. **f** Integration with AR glasses for immersive interaction in AR/VR scenarios

the jaw motions involved in pronouncing words, high jaw movements were employed. Furthermore, as shown in Fig. 5f, we connected the smartphone to AR glasses, enabling real-time display and interaction, which highlights the potential of RT-SSRS as a novel input modality for AR/VR applications and promotes the development of accessible and intelligent interaction technologies.

4 Conclusions

In summary, this paper presents a real-time silent speech recognition system (RT-SSRS) which can acquire and decode silent speech signals in real time. The triboelectric nanogenerator (TENG)-based flexible pressure sensor (FPS), worn on the chin, detects subtle jaw movements during speech

and converts them into electrical signals. Systematic characterization and optimization revealed that the outstanding performance of the FPS originates from its distinctive porous pyramid-structured silicone film (PPS) film, endowing it with high pressure sensitivity of 1 V N^{-1} for 0–10 N and 4.6 V N^{-1} for 10–24 N. Silent speech signals of 30 daily word categories were acquired and analyzed, revealing high similarity between classes, which demonstrates the necessity of using a neural network for accurate decoding. A hybrid deep learning framework CNN-LSTM was developed to accurately decode silent speech signals. This model achieving a classification accuracy of 95.83%, significantly outperforming the regular CNN model (90.28%). In practical human–machine interaction scenarios, the RT-SSRS enables precise and contactless control of smartphones through silent speech commands, offering a novel barrier-free communication method for individuals with speech impairments. Furthermore, by interfacing with AR glasses via smartphone, the system demonstrating strong potential for broader applications in AR/VR and related domains.

Acknowledgements This research was supported by the Natural Science Foundation of Fujian Province under Grant No. 2024J010016, Fujian Province Young and Middle aged Teacher Education Research Project No. JAT241317, and the Mindu Innovation Laboratory Project under Grant No. 2020ZZ113.

Author Contributions Shuai Lin contributed to data collection, formal analysis, investigation, and the writing of the original draft. Yanmin Guo contributed to data collection, formal analysis, and investigation. Xiangyao Zeng, Xiongtu Zhou, and Yongai Zhang involved with the formal analysis, investigation, resources, supervision, and validation. Chengda Li and Chaoxing Wu contributed to the conceptualization, formal analysis, resources, supervision, funding acquisition, and validation. All authors have read and agreed to the published version of the manuscript.

Declarations

Conflict of interest The authors declare no interest conflict. They have no known competing financial interests or personal relationships that could have appeared to influence the work reported in this paper.

Supplementary Information The online version contains supplementary material available at https://doi.org/10.1007/s40820-025-01982-z.

References

1. B.M. Jangabaevna, The significant role of language in the expression and transmission of emotions. Am. J. Philol. Sci. **5**(4), 93–95 (2025). https://doi.org/10.37547/ajps/Volume05Issue04-23
2. L. Wong, G. Grand, A.K. Lew, N.D. Goodman, V.K. Mansinghka, J. Andreas, J.B. Tenenbaum, from word models to world models: Translating from natural language to the probabilistic language of thought. arXiv preprint arXiv:2306.12672 (2023). https://doi.org/10.48550/arXiv.2306.12672
3. S.A. Teli, A.M. Sheikh, S. Jan, J.Y. Pala. Mir Language use during chatting and expressing emotions by Kashmiri speakers using whatsapp. J. South Asian Exch. 1(1) (2024). https://doi.org/10.21659/jsae/v1n1/v1n102
4. P. Hecker, N. Steckhan, F. Eyben, B.W. Schuller, B. Arnrich, Voice analysis for neurological disorder recognition-a systematic review and perspective on emerging trends. Front. Digit. Health **4**, 842301 (2022). https://doi.org/10.3389/fdgth.2022.842301
5. Y. Shevchenko, S. Dubiaha, O. Kovalova, H. Varina, H. Svyrydenko, Neuropsychological peculiarities of cognitive functions of speech-impaired junior pupils. Conhecimento Divers **15**(40), 322–339 (2023). https://doi.org/10.18316/rcd.v15i40.11252
6. A. Favaro, C. Motley, T. Cao, M. Iglesias, A. Butala et al., A multi-modal array of interpretable features to evaluate language and speech patterns in different neurological disorders. 2022 IEEE spoken language technology workshop (SLT), 532–539. IEEE (2023). https://doi.org/10.1109/SLT54892.2023.10022435
7. G.P. Usha, J.S.R. Alex, Speech assessment tool methods for speech impaired children: a systematic literature review on the state-of-the-art in speech impairment analysis. Multimed. Tools Appl. (2023). https://doi.org/10.1007/s11042-023-14913-0
8. C. Alighieri, K. De Maere, G. Poncelet, L. Willekens, C. Vander Linden et al., Occurrence of speech-language disorders in the acute phase following pediatric acquired brain injury: results from the Ghent university hospital. Brain Inj. **35**(8), 907–921 (2021). https://doi.org/10.1080/02699052.2021.1927185

9. A. Barman, A. Chatterjee, R. Bhide, Cognitive impairment and rehabilitation strategies after traumatic brain injury. Indian J. Psychol. Med. **38**(3), 172–181 (2016). https://doi.org/10.4103/0253-7176.183086
10. J. Leblanc, E. De Guise, M. Feyz, J. Lamoureux, Early prediction of language impairment following traumatic brain injury. Brain Inj. **20**(13–14), 1391–1401 (2006). https://doi.org/10.1080/02699050601081927
11. M.M. Smith, Simply a speech impairment? Literacy challenges for individuals with severe congenital speech impairments. Int. J. Disabil. Dev. Educ. **48**(4), 331–353 (2001). https://doi.org/10.1080/10349120120094257
12. C.P. Barnett, B.W.M. van Bon, Monogenic and chromosomal causes of isolated speech and language impairment. J. Med. Genet. **52**(11), 719–729 (2015). https://doi.org/10.1136/jmedgenet-2015-103161
13. K.P. Connaghan, C. Baylor, M. Romanczyk, J. Rickwood, G. Bedell, Communication and social interaction experiences of youths with congenital motor speech disorders. Am. J. Speech Lang. Pathol. **31**(6), 2609–2627 (2022). https://doi.org/10.1044/2022_AJSLP-22-00034
14. A. Dahlgren Sandberg, Phonological recoding problems in children with severe congenital speech impairments: the importance of productive speech. In: basic functions of language, reading and reading disability, pp. 315–327. Springer US (2002). https://doi.org/10.1007/978-1-4615-1011-6_19
15. R.K. Kadu, A.V. Chandak, P.J. Assudani, A. Tiwari, N. Jaurkar, Sign language recognition by hand gesture for deaf and speech impaired community using ML. 2024 OITS International conference on information technology (OCIT)., 542–547. IEEE (2025). https://doi.org/10.1109/OCIT65031.2024.00100
16. J.R. Green, C.A. Moore, K.J. Reilly, The sequential development of jaw and lip control for speech. J. Speech Lang. Hear. Res. **45**(1), 66–79 (2002). https://doi.org/10.1044/1092-4388(2002/005)
17. K.S. Talha, K. Wan, S.K. Za'ba, Z.M. Razlan, A.B. Shahriman, Speech analysis based on image information from lip movement. IOP Conf. Ser. Mater. Sci. Eng. **53**, 012016 (2013). https://doi.org/10.1088/1757-899x/53/1/012016
18. M. Bourguignon, M. Baart, E.C. Kapnoula, N. Molinaro, Lip-reading enables the brain to synthesize auditory features of unknown silent speech. J. Neurosci. **40**(5), 1053–1065 (2020). https://doi.org/10.1523/JNEUROSCI.1101-19.2019
19. M. Oghbaie, A. Sabaghi, K. Hashemifard, M. Akbari, When deep learning deciphers silent video: a survey on automatic deep lip reading. Multimed. Tools Appl. **84**(32), 40363–40405 (2025). https://doi.org/10.1007/s11042-024-20156-4
20. C. Yu, X. Wang, Z. Qian, Silent speech recognition using visual cascading fusion of tongue-lip movements based on pre-trained and fine-tuned model. EURASIP J. Audio Speech Music Process. **2025**(1), 16 (2025). https://doi.org/10.1186/s13636-025-00403-8
21. X. Wang, Z. Su, J. Rekimoto, Y. Zhang, Watch your mouth: silent speech recognition with depth sensing. Proceedings of the CHI conference on human factors in computing systems. Honolulu HI USA. ACM, 1–15. https://doi.org/10.1145/3613904.3642092
22. B. Huang, Y. Shao, H. Zhang, P. Wang, X. Chen et al., Design and implementation of a silent speech recognition system based on sEMG signals: a neural network approach. Biomed. Signal Process. Control **92**, 106052 (2024). https://doi.org/10.1016/j.bspc.2024.106052
23. Z. Li, B. Ma, W. Mao, J. Zhang, Z. Yu et al., SVIT-SSR: a sEMG-based vision transformer approach for silent speech recognition. Electron. Lett. **60**(21), e13285 (2024). https://doi.org/10.1049/ell2.13285
24. J. Menezes, C. Wagner, P. Steiner, P. Schaffer, D. Plettemeier et al., Non-invasive speaker-dependent continuous phoneme recognition with a radar-based silent speech interface. ICASSP 2025 - 2025 IEEE international conference on acoustics, speech and signal processing (ICASSP), 1–5. IEEE (2025). https://doi.org/10.1109/ICASSP49660.2025.10887719
25. J. Menezes, M. Schütze, P. Schaffer, D. Plettemeier, P. Birkholz, Exploring antenna placement configurations with a radar-based silent speech interface. ICASSP 2025 - 2025 IEEE international conference on acoustics, speech and signal processing (ICASSP), 1–5. IEEE (2025). https://doi.org/10.1109/ICASSP49660.2025.10890284
26. G. Zhu, C. Pan, W. Guo, C.-Y. Chen, Y. Zhou et al., Triboelectric-generator-driven pulse electrodeposition for micropatterning. Nano Lett. **12**(9), 4960–4965 (2012). https://doi.org/10.1021/nl302560k
27. F.-R. Fan, Z.-Q. Tian, Z.L. Wang, Flexible triboelectric generator. Nano Energy **1**(2), 328–334 (2012). https://doi.org/10.1016/j.nanoen.2012.01.004
28. S. Fu, W. He, H. Wu, C. Shan, Y. Du et al., High output performance and ultra-durable DC output for triboelectric nanogenerator inspired by primary cell. Nano-Micro Lett. **14**(1), 155 (2022). https://doi.org/10.1007/s40820-022-00898-2
29. K.-H. Lee, M.-G. Kim, W. Kang, H.-M. Park, Y. Cho et al., Pulse-charging energy storage for triboelectric nanogenerator based on frequency modulation. Nano-Micro Lett. **17**(1), 210 (2025). https://doi.org/10.1007/s40820-025-01714-3
30. G. Du, J. Zhao, Y. Shao, T. Liu, B. Luo et al., A self-damping triboelectric tactile patch for self-powered wearable electronics. eScience **5**(2), 100324 (2025). https://doi.org/10.1016/j.esci.2024.100324
31. B. Shi, Q. Wang, H. Su, J. Li, B. Xie et al., Progress in recent research on the design and use of triboelectric nanogenerators for harvesting wind energy. Nano Energy **116**, 108789 (2023). https://doi.org/10.1016/j.nanoen.2023.108789
32. Z. Zhao, Z. Quan, H. Tang, Q. Xu, H. Zhao et al., A broad range triboelectric stiffness sensor for variable inclusions recognition. Nano-Micro Lett. **15**(1), 233 (2023). https://doi.org/10.1007/s40820-023-01201-7
33. Z. Xu, D. Li, K. Wang, Y. Liu, J. Wang et al., Stomatopod-inspired integrate-and-fire triboelectric nanogenerator for harvesting mechanical energy with ultralow vibration speed. Appl. Energy **312**, 118739 (2022). https://doi.org/10.1016/j.apenergy.2022.118739

34. K. Wang, Y. Weng, G. Chen, C. Wu, J.H. Park et al., Coupling electrostatic induction and global electron circulation for constant-current triboelectric nanogenerators. Nano Energy **85**, 105929 (2021). https://doi.org/10.1016/j.nanoen.2021.105929
35. Y. Wang, Z. Gao, W. Wu, Y. Xiong, J. Luo et al., TENG-boosted smart sports with energy autonomy and digital intelligence. Nano-Micro Lett. **17**(1), 265 (2025). https://doi.org/10.1007/s40820-025-01778-1
36. W. Chen, J. Kang, J. Zhang, Y. Zhang, X. Zhou et al., An information display and encrypted transmission system based on a triboelectric nanogenerator and a cholesteric liquid crystal. Nano Energy **134**, 110594 (2025). https://doi.org/10.1016/j.nanoen.2024.110594
37. W. Dong, K. Sheng, B. Huang, K. Xiong, K. Liu et al., Stretchable self-powered TENG sensor array for human-robot interaction based on conductive ionic gels and LSTM neural network. IEEE Sens. J. **24**(22), 37962–37969 (2024). https://doi.org/10.1109/JSEN.2024.3464633
38. S. Jiang, X. Liu, J. Liu, D. Ye, Y. Duan et al., Flexible metamaterial electronics. Adv. Mater. **34**(52), 2200070 (2022). https://doi.org/10.1002/adma.202200070
39. F.-R. Fan, L. Lin, G. Zhu, W. Wu, R. Zhang et al., Transparent triboelectric nanogenerators and self-powered pressure sensors based on micropatterned plastic films. Nano Lett. **12**(6), 3109–3114 (2012). https://doi.org/10.1021/nl300988z
40. Y. Qin, X. Ma, Z. Ruan, X. Xiang, Z. Shi et al., Improvement of thermal stability of charges in polylactic acid electret films for biodegradable electromechanical sensors. ACS Appl. Mater. Interfaces **16**(45), 62680–62692 (2024). https://doi.org/10.1021/acsami.4c13772
41. P. Zhang, Y. Ma, H. Zhang, L. Deng, High-performance triboelectric nanogenerators based on foaming agent-modified porous PDMS films with multiple pore sizes. ACS Appl. Energy Mater. **6**(12), 6598–6606 (2023). https://doi.org/10.1021/acsaem.3c00633

 https://doi.org/10.1007/s40820-025-01982-z